

Ultra-light h-BCN architectures derived from new organic monomer with tunable electromagnetic wave absorption

Tao Zhang ^{a,1}, Jian Zhang ^{a,1}, Guangwu Wen ^a, Bo Zhong ^a, Long Xia ^{a,*},
Xiaoxiao Huang ^{b,**}, Hu Zhao ^c, Huatao Wang ^a, Luchang Qin ^d

^a School of Materials Science and Engineering, Harbin Institute of Technology (Weihai), Weihai, 264209, PR China

^b School of Materials Science and Engineering, Harbin Institute of Technology, Harbin, 150001, PR China

^c School of Materials, University of Manchester, Oxford Road, Manchester, M13 9PL, UK

^d Department of Physics and Astronomy, University of North Carolina at Chapel Hill, Chapel Hill, NC, 27599-3255, USA



ARTICLE INFO

Article history:

Received 23 November 2017

Received in revised form

27 April 2018

Accepted 1 May 2018

Available online 4 May 2018

ABSTRACT

Hexagonal BCN (h-BCN) has been identified as a promising class of electromagnetic wave (EMW) absorption material for critical Mach number aerocraft due to its exceptional thermal and chemical stabilities as well as adjustable dielectric property. Herein, we report a facile precursor synthesis-pyrolysis method to obtain ultra-light h-BCN bulk ceramics and microtubes (MTs) using commercially available BCl_3 , ethylenediamine and aniline as the monomers. The h-BCN bulk with a density of 15 mg/cm^3 can be in situ synthesized derived from the precursor located in a tube furnace, while h-BCN MTs are simultaneously obtained on the downstream graphite sheets by controlling the pyrolysis temperature at the wide range of $800\text{--}1200^\circ\text{C}$. For the h-BCN bulk ceramics, the minimum reflection loss (RL) can be tailored by controlling the N dopants, ranging from -52.7 dB at 5.44 GHz (the band width below -10 dB is achieved in a wide frequency range from 2.8 to 18 GHz) to -20.6 dB at 14.8 GHz (the band width below -10 dB is narrowed from 13.4 to 18 GHz). The excellent and frequency-controllable microwave absorption properties are due to the combination of tunable complex permittivity and lattice polarization resulting from B and N dopants in carbon networks.

© 2018 Elsevier Ltd. All rights reserved.

1. Introduction

With the widespread application of EMW, the band width of EMW for civilian and military uses has become wider and wider. Thus, EMW absorption materials of the new generation face new challenges versus traditional absorbents. As for high speed aerocraft (especially critical Mach number aerocraft), the EMW absorption materials with higher temperature stability, lower density and tunable EMW absorption properties are critically needed [1]. Typically, EMW absorbing materials can be generally classified into magnetic and dielectric materials. Even though magnetic particles absorbents exhibit excellent EMW absorption property, they have the unavoidable high density, such as Ni, Co, Fe, Nd-Fe-B or their alloys and ferrite. For dielectric materials, carbon-based absorbents

are representative; additionally, in order to improve the performance of EMW absorption and lower the density, many researchers introduce magnetic ingredient into carbon-based materials to synthesize carbon-based composites, such as graphene filled with magnetic particles [2–4], modified carbon nanotubes [5–7], modified carbon nanofibers [8,9] and porous carbon decorated with magnetic particles [10–13]. However, both these magnetic and dielectric materials cannot withstand high temperature and few have tunability. Carbon-based absorbents will be oxidized above 550°C in ambient atmosphere. And magnetic particles can be demagnetized below 780°C because the Curie's temperature of decorated magnetic particles is generally below 780°C [14,15]. Whence these widely reported magnetic and dielectric materials are inefficient for high temperature EMW absorption (especially above 850°C).

According to the reported works, silicon dopant has been proposed on the fabrication of SiC nanowires [16–18], nanofibers [19], core-shell particles [20] and nanotubes [17,21]. Despite the SiC architectures exhibit excellent high temperature stability and

* Corresponding author.

** Corresponding author.

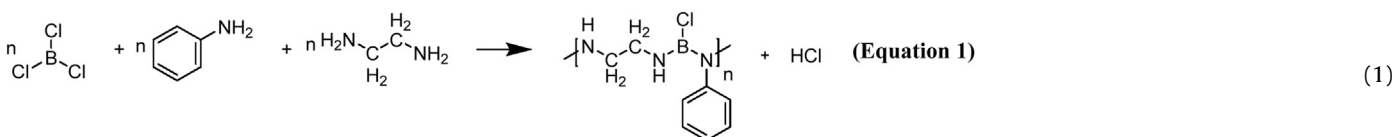
E-mail addresses: xialonghit@gmail.com (L. Xia), swliza@hit.edu.cn (X. Huang).

¹ Tao Zhang and Jian Zhang contributed equally to this work.

improved EMW absorption, the complex permittivity of SiC cannot be tailored and the effective absorption frequency is usually at relatively higher GHz due to the weak polarization of Si-C bonds [16]. In this scenario, however, boron and nitrogen are ideal dopants for low-density (even lower than carbon and SiC), high thermostability and strong polarization which can improve the EMW absorption. Moreover, the complex permittivity of h-BCN materials can be tailored by adjusting the B: N: C atom ratio and the band gaps are known to be intermediate between conductive graphite and insulating hexagonal BN [22,23]. Therefore, the dielectric properties of h-BCN materials can be more easily controlled by adjusting their chemical composition and the configuration of B, C, and N atoms in the hexagonal lattice rather than by oxidizing control in pure carbon materials [24,25]. The facile and large-scale preparation of heteroatom doped hybrid-carbon architectures with high thermostability and low-density is the theoretical and tech-

trichloride (BCl_3), aniline and ethylenediamine through the possible chemical reaction (Equation (1)). Gaseous BCl_3 was piped into a three-neck flask with a flow rate of 0.35 L/min which contained the mixture of aniline and ethylenediamine (the ratios are compiled in Table 1) and was heated at 95 °C by water bath for 3 h. After that, the products were slowly cooled to the room temperature in ambient condition and showed egg-yolk-like color with sticky features. The synthesized precursors in different molar ratios were marked as P1, P2 and P3, compiled in Table 1.

BCl_3 (purity 99.9%) was purchased from Guangzhou Ruihe Chemical Science and Tech. Co. Ltd. (Guangzhou, China). Aniline ($\text{Ph}-\text{NH}_2$, purity ≥ 98%) was obtained from Tianjin Yongda Chemical Reagent Co. Ltd. (Tianjin, China). Ethylenediamine (purity ≥ 99.0%) was obtained from Tianjin Gaoyu Fine Chemical Co. Ltd. (Tianjin, China). Deionized water was produced by a Millipore-ELIX water purification system in all the experiments.



nical challenges toward the creation of a new type of EMW absorbent [21,26,27]. Furthermore, in the reported literature, a series of methods including precursor pyrolysis [28], laser ablation [29], hot-filament chemical vapor deposition (CVD) [30,31], laser vaporization process, aerosol-assisted CVD [32] and arc discharge [33] using different B, C and N sources, have been studied for the synthesis of BCN different architectures. Among the fabrication methods mentioned above, organic precursor polymerization and pyrolysis method is an ideal process to obtain BCN products due to the designable molecule structures. Moreover, it is delighted that precursor pyrolysis is a facile, economical and composition-controllable method for large-scale synthesis of bulk ceramics or microstructures [34–36].

Herein, large-scale h-BCN bulk ceramics and MTs are simultaneously synthesized using BCl_3 , ethylenediamine and aniline as the monomers. Atomic ratio of B: C: N of the synthesized h-BCN can be controlled by adjusting the molar ratio of the raw reactants of the precursors. Then we computerize the h-BCN models on the basis of the First-Principles theory (CASTEP analysis) to predict the electron polarization behavior and band gaps of h-BCN. Furthermore, the executed examinations of the electromagnetic parameters verify the tunabilities of the complex permittivity and the minimum RL through heteroatom doping and polarization engineering (i.e., doped with B and N in carbon lattice). Finally, we study the EMW absorption properties of the h-BCN bulk ceramics in comparison with h-BCN MTs and propose potential applications of this new hybrid ceramics in high temperature absorbents and shielding materials. The possible EMW absorption and the growth mechanism for h-BCN are proposed and explored as well.

2. Experimental

The organic precursor was synthesized by using the Boron

The as-prepared precursor was put into a boat-shaped crucible on the upstream and a piece of graphite paper (60×35 mm), acted as a substrate, was put on the downstream in a tube furnace protected by flowing Ar (purity 99.999%, flowing rate 0.30 L/min). The heating modes are compiled in Table 2 (H1 H2 and H3). Finally, the products of h-BCN bulk and MTs were simultaneously collected from the crucible and graphite paper, respectively, without any further purification.

An optical contact angle instrument (JC 2000D) was used to measure the contact angle and this instrument was carried out by sessile drop technique, whose droplets were produced by micro-syringe. From the captured images, the angle of liquid-solid interface was measured by Goniometry. The present first principle calculations were carried out using ultrasoft pseudopotentials and local density approximation (LDA) in Cambridge Sequential Total Energy Package (CASTEP) code of Materials Studio software (version 8.0), which is a typical software to calculate the energy and electromagnetic properties of a crystal cell based on Schrödinger equation. After the calculation, the complex permittivity (ϵ' , ϵ'') can be directly analyzed from calculation results of the CASTEP by analyzing the optical properties utilizing Materials Studio. The kinetic energy cutoff is 310 eV and the sets of k-points are $4 \times 5 \times 3$ separation of 0.04 \AA^{-1} [37], $8 \times 10 \times 6$ separation of 0.04 \AA^{-1} and $10 \times 12 \times 7$ separation of 0.04 \AA^{-1} . The morphologies of the synthesized samples were characterized by a MX2600FE field emission scanning electron microscope (FESEM) equipped with an energy dispersive spectrometer (EDS). The micro-structure of the pyrolyzed products was determined by transmission electron microscope (TEM) and high resolution transmission electron microscopy (HRTEM, Tecnai F30 FEG) equipped with an energy dispersive X-ray

Table 2
Heating modes of sintering.

Heating modes	H1	H2	H3
Heating rates	5 °C/min	3 °C/min	3 °C/min
Maximum temperature	1200 °C	At 600 °C for 1 h	1000 °C
Heating profile			
Cooling profile	Above 600 °C: 5 °C/min to 600 °C Below 600 °C: By furnace cooling		

Table 1
Types of precursors with different molar ratios of reactants.

Precursor types	P1	P2	P3
Molar ratios (Aniline: Ethylenediamine)	1: 0.5	1: 1.25	1: 2

spectroscopy (EDS). The crystalline structure was detected by using Rigaku D/Max 2000 VPC powder X-ray diffractometer (XRD, CuK α radiation, $\lambda = 1.45418 \text{ \AA}$). Raman spectroscopy (Renishaw, RM-1000) was used to characterize the structure of the h-BCN bulk at 532 nm laser excitation. The chemical characteristics were examined by Fourier transform infrared (FTIR, Bruker VECTOR-22). The Barrett-Emmett-Teller (BET) surface area was performed at 77 K using nitrogen in a conventional volumetric method by Micromeritics ASAP 2020. Thermogravimetric analysis (TGA) was carried out on a NETZSCH STA 449C under N₂ atmosphere. X-ray photoelectron spectroscopic measurements were performed on a Thermal Scientific ESCALAB 250X using a monochromatic Al X-ray source. The complex permittivity (ϵ_r) and complex permeability (μ_r) values were measured by a vector network analyzer (Agilent N5245A) with precision mechanical calibration kit (Agilent 85050C) in the range of 2–18 GHz to evaluate microwave absorption properties. The composite samples for EMW absorption measurement were prepared by mixing the product with paraffin wax (the chemical composition was C₂₅H₅₂; the density 0.87 g cm⁻³; the melting temperature 49 °C; and the heat capacity 2.2 J g⁻¹ K⁻¹) in a mass ratio of 1:5. The mixing process was as follows. 0.5 g paraffin wax was heated to 60 °C in a watch glass to form a transparent liquid. 0.1 g h-BCN powder was introduced into the wax liquid and

ultrasonically dispersed for 20 min at 60 °C. Then the mixture was cooled down to room temperature forming a black composite bulk. The composite was pressed into a steel mold to shape a cylinder with an inner diameter of 3.0 mm and outer diameter of 7.0 mm. After that, the composite samples were measured by co-axial line from 2 to 18 GHz.

3. Results and discussion

3.1. Calculation and theoretical prediction of EMW absorption performance

We have reported that the h-BCN ternary compound had an excellent performance in EMW absorption [38,39]. Additionally, according to the reported investigation, the polarization among electrons will contribute to the enhanced EMW absorption properties [15,40–43]. Thus, in this paper, we calculated the electron density of the h-BCN ternary compound (Fig. 1a–d) by CASTEP, showing that the density of electron cloud is asymmetry due to the ratio of N dopants in carbon networks. Considering the difference of electronegativity among B, C and N (N > C > B), this phenomenon implies the existence of electronic polarization or interfacial polarization which both could critically interact with the incident

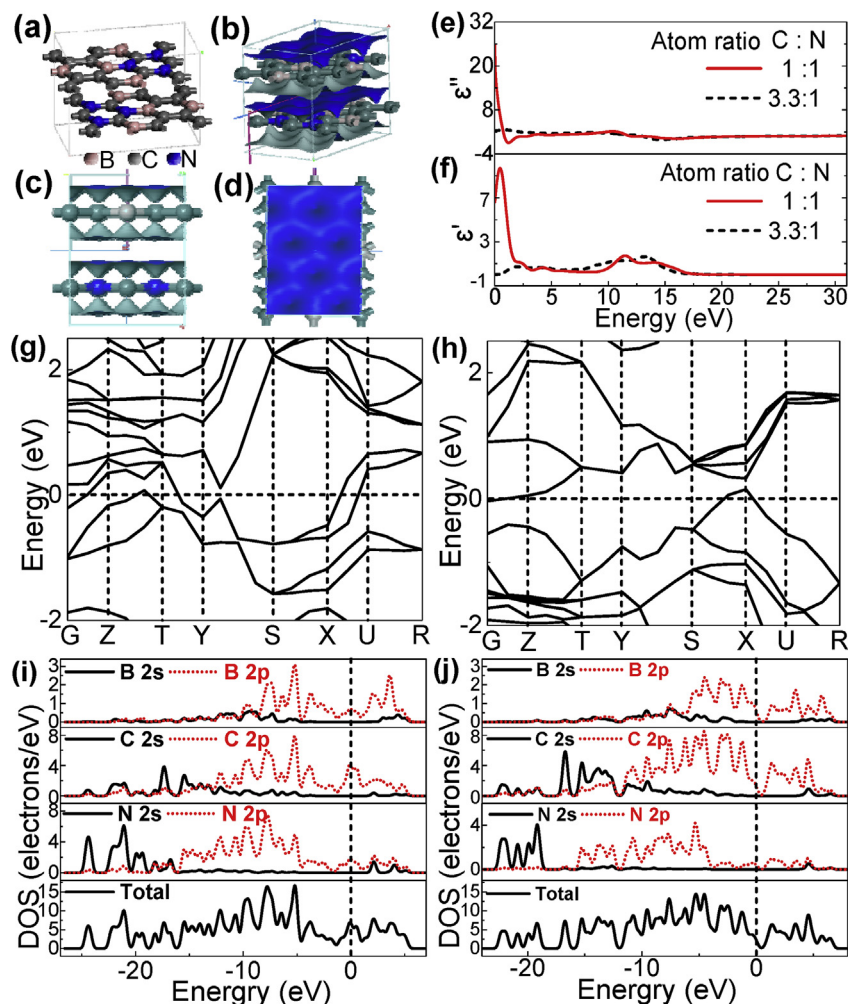


Fig. 1. Calculation to predict the performance of EMW absorption by CASTEP. (a)–(d) The electron density of h-BCN showing uneven properties of electrons. The imaginary part ϵ'' (e) and real part ϵ' (f) of complex permittivity parameters for BCN with different atom ratios between Carbon and Nitrogen (1: 1 and 3.3: 1, respectively). (g, h) Band structure (partly) of h-BCN with different atom ratios between Carbon and Nitrogen (1: 1 and 3.3: 1, respectively). (i, j) Total and partial DOS of h-BCN with different atom ratios between Carbon and Nitrogen (1: 1 and 3.3: 1, respectively). In partial of DOS of B, C and N atoms, solid and dashed lines represent s and p orbitals, respectively.

EMW. Fig. 1e and f shows the computerized results of the complex permittivity ($\epsilon_r = \epsilon' - j\epsilon''$) with two type of atom ratios between C and N. According to Planck-Einstein relation ($E_{in} = h\nu$, where, E_{in} is energy of the incident wave, h is the Plank constant, ν is the frequency of incident EMW), when the energy of incident EMW (E_{in}) is low, comparing with the lower content of N dopants (3:3:1, black dot-line showing in Fig. 1e and f), the higher content of N dopants (1:1, red line showing in Fig. 1e and f) shows a relative higher value of ϵ' and ϵ'' . Particularly, this study focuses on the frequency from 2 to 18 GHz, corresponding to the energy from 8.27×10^{-6} to 7.44×10^{-5} eV. Therefore, doping N in carbon networks can both raise ϵ' and ϵ'' . Fig. 1g and h shows the band structures of h-BCN with aforementioned atom ratios respectively. There both appear orbits crossing the Fermi level, implying the dominative hole-conductivity [37]. As shown in Fig. 2i and j, the partial densities of states for each atom (B, C and N), as well as the total densities of states for these two types of h-BCN, have been calculated. To make sure the results are creditable, the calculations were repeated with higher K-points mesh ($8 \times 10 \times 6$ and $10 \times 12 \times 7$) and the calculated results are unchanging. From Fig. 1i (the atomic ratio 1:1 of C:N), the valence bands between -26.0 eV and -16.0 eV are mainly contributed by N s orbitals and C s orbitals, but B s and p orbitals have minimum contributions. The valence bands between -16.0 eV and 0.0 eV are mainly contributed by N p orbitals and C p orbitals, but B p orbitals have relatively minimum contributions. The conduction band is mainly contributed by C p, N p and B p orbitals (Fig. 1j). The states in the Fermi level consist mostly of C and N p orbitals, where the C and N atoms contribute 3.82 and 1.73 electron/eV, respectively. The rest states from B atoms are only 0.70 electron/eV. As shown in Fig. 1j (the atomic ratio 3:3:1 of C and N), the valence bands between -24.0 eV and -15.0 eV are mainly from N and C s orbitals, but B s and p orbitals have minimum contributions as well. The valence bands between -12.0 eV and 0.0 eV are mainly from N and C p orbitals, while B p orbitals make relatively small contributions. The conduction band mainly be contributed by C and B s orbitals,

whereas N p orbitals make a small contribution. The states in the Fermi level consist mostly of C p orbitals, whose contribution is 1.27 electron/eV. The rest are from B atoms with 0.06 electron/eV and N atoms with 0.40 electron/eV. From Fig. 1i and j, when N atom ratio between C and N is raised from 3:3:1 to 1:1:1, the density of states (DOS) at the Fermi level increase from 1.73 electron/eV to 6.25 electron/eV accordingly, which indicates the enhancement of electrical conductivity (σ).

In alternating electric field, the complex permittivity can be represented as $\epsilon_r = \epsilon' - j\epsilon''$. In this equation, the real part (ϵ') and the imaginary part (ϵ'') represent the ability of energy storage and dissipation, respectively [27]. For the imaginary part (ϵ''), it is determined by the following two factors [44,45].

$$\epsilon'' = \frac{\sigma_{dc}}{\omega\epsilon_0} + \epsilon''_{ac} \quad (2)$$

where, σ_{dc} is the DC conductivity, ω is the angular frequency, ϵ_0 is the permittivity of free space, and ϵ''_{ac} is the dielectric loss contribution. From aforementioned analysis, the enhancement of N ratio in this ternary h-BCN compound can theoretically improve the performance in the absorption of EMW.

3.2. Preparation process, morphology, chemical analysis and microstructure of h-BCN bulks and h-BCN MTs

Fig. 2a shows the synthesis process and the photograph of the organic precursor. A mass of hydrogen bonds (between N-H and C-H) exist in the raw materials and the expected precursors, which would generate a dramatic increase in complexation strength [46]. Therefore, the reactive monomers and the units of the precursor can be constrained in an exact space to some degree which is of great benefit to form B-C-N hybrid rings. In the molecular scale, the possible crosslinking reaction to form inorganic hexagonal BCN bulk by annealing is shown in Fig. 2b and c. The crosslinking reaction, which is accompanied with some elimination reactions (–H,

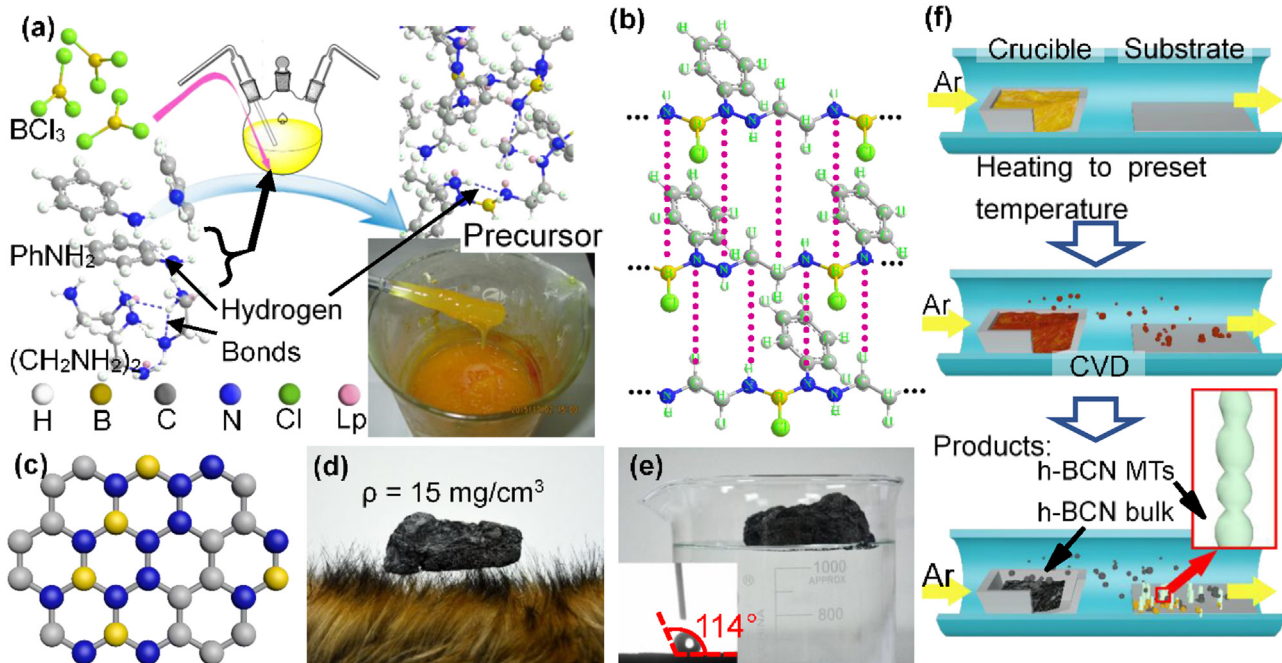


Fig. 2. Preparation pathway of the precursor, h-BCN bulk and MTs. (a) Synthesis process of h-BCN precursor. (b, c) Possible reaction process of the h-BCN formation by using the organic precursor. (d) Digital photograph of ultra-light h-BCN bulk ceramics above the zirconia fur. (e) Floating above the water and the contact angle of h-BCN bulk. (f) Schematic layout of the CVD setup for the formation and growth of h-BCN bulk and MTs.

-Cl and part of $-\text{NH}_2$), produces hybrid h-BCN bulk with the byproducts of HCl or NH_4Cl during annealing stage (Fig. 2c). The prepared h-BCN bulk (Fig. 2d) can be easily buttressed by zirconia fur suggesting the quite low density (15 mg/cm^3), as good as the reported nanotube aerogels synthesized by Kim et al. [47]. In addition, the water wetting property of the h-BCN bulk was conducted by contact angle measurement (inset of Fig. 2e) which shows that the water contact angle is about 114° . Moreover, in Fig. 2e, the h-BCN bulk can float on the water surface further indicating the light-weight and superhydrophobic properties similar to the reported BN films [48]. Fig. 2f shows the schematic layout of the atmospheric pressure CVD used to synthesize h-BCN MTs. The CVD process could be roughly divided into three stages including stage 1 in which the precursor is heated to the preset temperature (the precursor in the crucible on the upstream and a piece of graphite paper on the downstream in a furnace tube), stage 2 in which the precursor is vaporized and then solidified on the graphene paper to form h-BCN MTs, and stage 3 in which the precursor is shrunk and h-BCN MTs grow longer. The formation of the h-BCN MTs could be assigned to a vapor-phase mechanism with a supersaturation-nucleation process by utilizing “droplet epitaxy” [49]. The structure and state evolutions of the precursor occur simultaneously during the whole annealing process and the color of precursor gradually changes from yellow, brown to black.

Fig. 3a–c shows the SEM images of the h-BCN bulks with the same heating mode H1 but different types of precursors (P1, P2 and P3, respectively) whose molar ratios of ethylenediamine increase in sequences from P1 to P3. Comparing the three images, it is noteworthy that the morphology of these h-BCN shows up a tendency that increasing the ethylenediamine ratios obviously inclines to form lamellar structures. Fig. 3d–f shows the morphology of h-BCN bulks which originated from the same precursors with Fig. 3a–c, respectively, but they were all annealed under different heating mode (H2). Fig. 3d–f shows that the h-BCN bulks are constructed by the curved nanoflakes which are more than $100 \mu\text{m}$ in diameter and several nanometers in thickness. All the three samples exhibit similar microstructures even though the precursor compositions vary from P1 to P3. Whereas the heating rates with different heating modes (H1 and H2) make significant contributions to the formation of lamellar structures by crossing contrast (Fig. 3a and d, Fig. 3b and e, Fig. 3c and f, respectively), indicating that slower heating rate could contribute to growth of intact h-BCN nanoflakes. As mentioned above, the increasing ratios of ethylenediamine and the slow heating rates are conclusively favored for the formation of the lamellar structure.

Fig. 4 shows the formation process of h-BCN bulks grown at different temperatures. Fig. 4a shows the featureless morphology of the sample annealed at 600°C with large pores ($2\text{--}5 \mu\text{m}$) in the

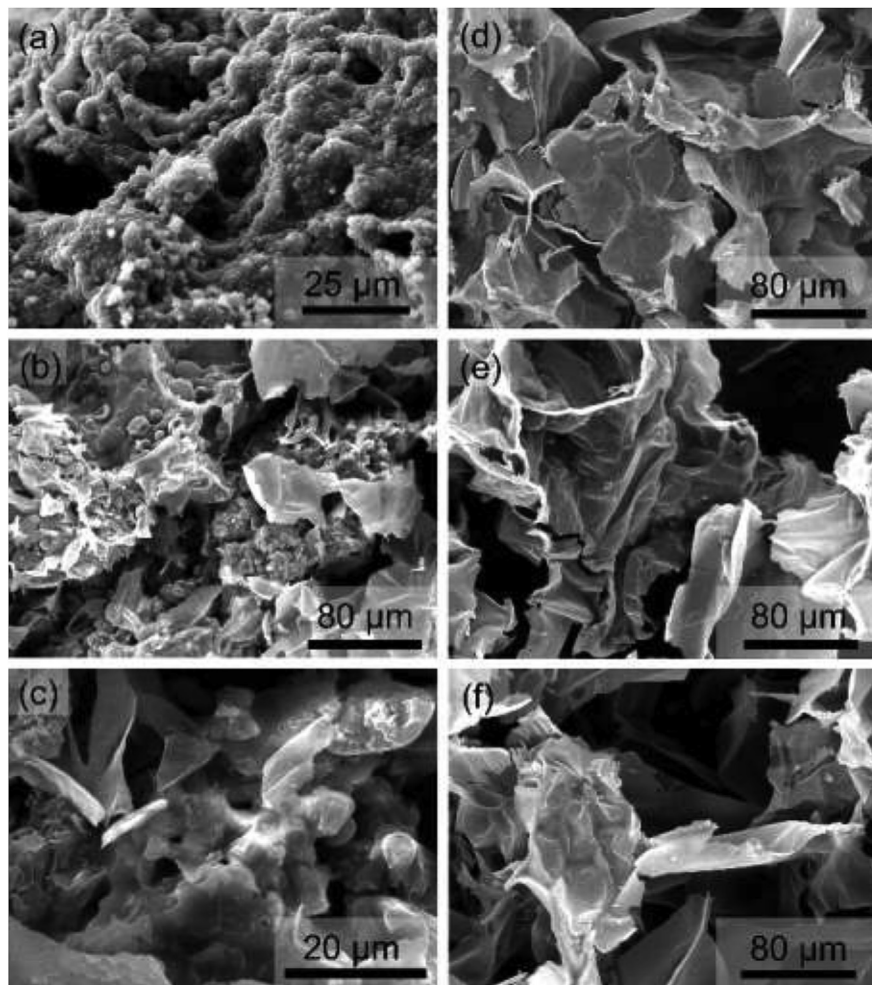


Fig. 3. High resolution SEM images of h-BCN bulks with different types of precursors and heating modes showing the morphology changes with different molar ratios and different heating rates. (a)–(c) SEM images of h-BCN bulks sintered by H1 heating mode with P1, P2 and P3 precursors, respectively. **(d)–(f)** SEM images of h-BCN bulks sintered by H2 heating mode with P1, P2 and P3 precursors, respectively.

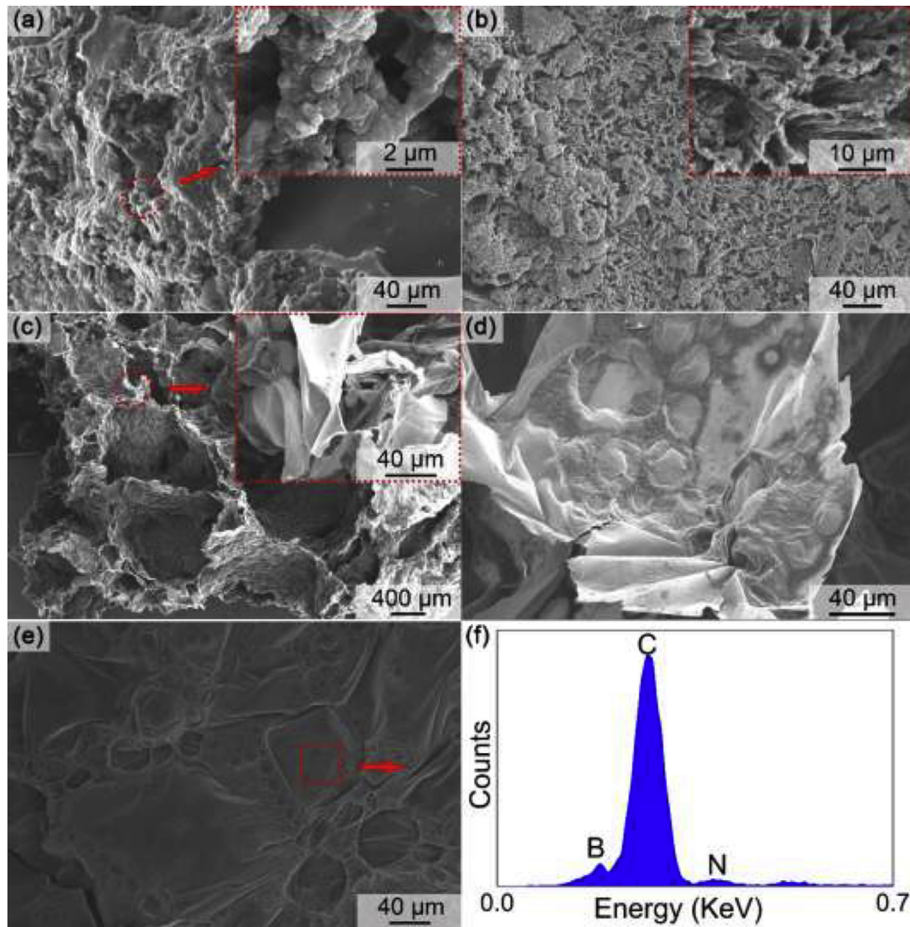


Fig. 4. SEM images of h-BCN bulks and its chemical compositions. SEM images of h-BCN bulk prepared at (a) 600 °C, (b) 800 °C, (c, d) 1000 °C and (e) 1200 °C. (f) The EDS spectrum of h-BCN bulk.

structure. When the temperature reaches 800 °C (Fig. 4b), large quantities of regular branch-like pores (2–10 μm) are observed due to the elimination of volatile chemical groups (NH₂, Cl, H et al.) possibly. When the temperature approaches to 1000 °C (Fig. 4c), due to the accelerated pyrolysis reaction at relatively higher temperature, the above-mentioned branch like pores grow much larger (100–200 μm) constructed by large amounts of curved nanoflakes (inset of Fig. 4c and d). When the annealing temperature is raised to 1200 °C (Fig. 4e), the diameters of former larger pores almost tend to be stable in size but the walls' surfaces of the pores show a relative smoother characteristic with many shrivelled bubbles (Fig. 4e versus 4d) because the gaseous chemical groups volatilize violently at higher temperature. The hexagonal structure could be responsible for the formation of the nanoflakes which is similar with the growth of graphene [50,51]. Many shrivelled bubbles are observed in the h-BCN nanoflakes which could indicate the processes of melting, evaporation and solidification. Fig. 4f manifests the component elements of B, C and N and no other elements are detected suggesting the purity of the as-prepared products.

Because of the existence of the vaporization stage in pyrolytic process of the precursor, the formation of large amounts of h-BCN MTs takes place upon the substrate lied on the downstream of the tube furnace. Fig. S1 a-c (Supporting Information) show the typical SEM images of h-BCN MTs, grown at different temperatures with apparently different morphologies. In Fig. S1 a, when the temperature reaches to 800 °C, the deposited products have inhomogeneous morphology. The Zig-zag and straight tubes are observed in

the same products with the diameter about 0.6 μm and 0.3 μm respectively. The h-BCN MTs grown at 800 °C show a relatively impure appearance, whereas, a very good purity is observed for the products grown at 1200 °C (Fig. S1 b). Fig. S1 b and c, when the temperature is raised to 1200 °C, pretty homogeneous h-BCN MTs with high packing densities are observed, which exhibit a heliciform and curly appearance and whose diameters become larger (0.5–1.0 μm). Additionally, these two kinds as-synthesized h-BCN MTs have different transparencies according to the high magnification images which reveal the different wall thicknesses of h-BCN MTs; the h-BCN MTs prepared at higher temperature exhibit a poor transparency, indicating the higher temperature can lead to thicker walls. Therefore, as mentioned above, a relatively higher temperature can be contributed to pure and homogeneous products but it also can lead to a curly morphology. Fig. S1 d shows the EDS spectrum from the selected spot shown in Fig. S1 c, indicating the main component elements B, C and N (the O peak, it is possibly caused by the moisture absorption in the ambient).

The morphologies of h-BCN MTs prepared at different heating rates are also studied. Fig. 5a and b shows the low and high magnification images of h-BCN MTs annealed at H1 heating mode (5 °C/min) and Fig. 5c and d shows the images annealed at H2 heating mode (3 °C/min). In Fig. 5a and b, large amounts of homogeneous and pure h-BCN MTs without any other impurities are observed at H1 and the average length is more than 100 μm. The hollow structure of the bamboo-like h-BCN MTs can be clearly observed according to the cross section morphology (inset of

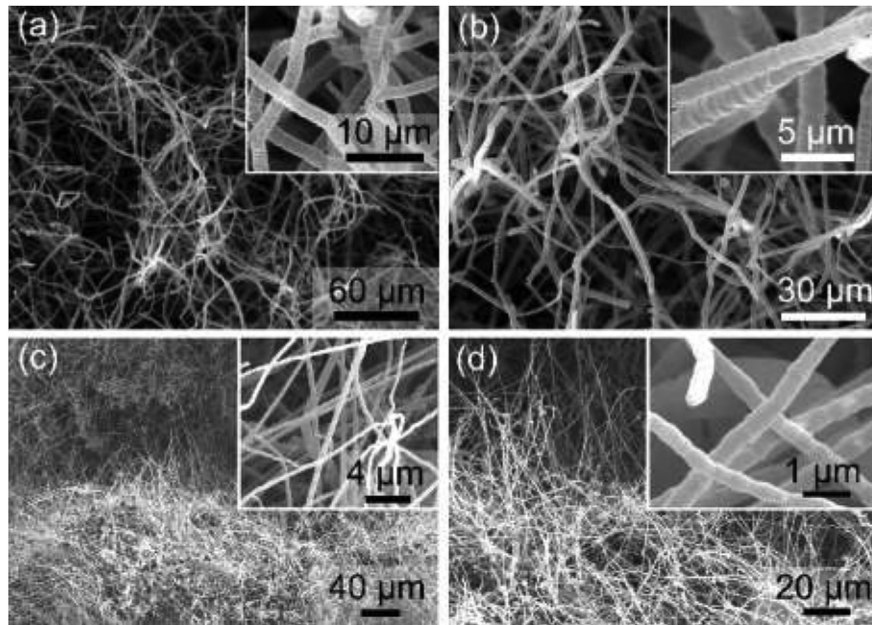


Fig. 5. SEM images of h-BCN MTs synthesized at different heating modes: (a, b) H1 heating mode. (c, d) H2 heating mode.

Fig. 5a) with the diameter about 2.0–3.0 μm . In **Fig. 5c** and **d**, the lengths and the diameters of these h-BCN MTs prepared at H2 are more uniform (the average length is 100 μm and the average diameter is 0.7 μm) than the products prepared at H1. Comparing these two kinds of h-BCN MTs, it is interesting that they both have high packing densities but have differences in the entire length, diameter and the average joint length. The products would grow up with shorter joint lengths and entire tube lengths but larger diameters (inset of **Fig. 5a** and **b**) annealed at the higher heating rate (H1), while under the lower heating rate (H2), the products would grow up with longer joint lengths and entire tube lengths but smaller diameters (**Fig. 5c** and **d**).

Fig. S2 shows the HRTEM images of micro-nano structures of h-BCN bulk annealed at H3 heating mode (**Fig. S2 a–c**) and h-BCN microtubes annealed at H1 heating mode (**Fig. S2 d–f**) and H2 heating mode (**Fig. S2 g–i**). For the h-BCN bulk, in **Fig. S2 a**, the organdie-like h-BCN sample shows a bending and scrolling appearance and it can be clearly observed some tiny nanoflakes inside. **Fig. S2 b** and **c** are the HRTEM images showing rectangular regions in **Fig. S2 a** and the highly ordered lattice fringes can be observed clearly. The interplanar spacing is 0.368 nm, corresponding to (002) planes of h-BCN (**Fig. S2 b**). **Fig. S2 d** shows the morphological and structural characterizations of the h-BCN MTs which are constructed by numerous graphene-like sheets with bamboo-like morphology. In **Fig. S2 e**, the SAED pattern of the MTs in **Fig. S2 d**, whose rings can be indexed to the (002), (100) and (004) diffractions of h-BCN respectively, reveals the hexagonal structure characteristics. Sharp lattice fringes (**Fig. S2 f**) are observed and the distance of the adjacent layers is 0.381 nm slightly larger than h-BCN bulk. In **Fig. S2 g** and **h** clearly show that the h-BCN MTs prepared at H1 heating mode have a thicker walls and thinner chamber (versus **Fig. S2 d**). The interplanar spacing (**Fig. S2 i**) is 0.355 nm which is the smallest in the three h-BCN structures. These aforementioned three different interlayer distances are quite close to the d_{002} of h-BCN (~3.420 nm), reveals that these annealed products have the same hexagonal lattice structure and the differences of the distances are possibly caused by the B and N dopants in graphitic layers. **Fig. S2 k** and **l** display the corresponding EDS mapping of C and N elements with different colors

from **Fig. S2 j**. It can be seen that both C and N elements uniformly distribute throughout the entire MTs. The positions of the individual B element have not been identified, owing to the deficiency of equipment's distinguishability for light elements (from ${}^1\text{H}$ to ${}^5\text{B}$).

Fig. 6a and **b** exhibit the XRD patterns of the samples derived from different types of precursors (P1, P2 and P3) at the same temperature (500 $^\circ\text{C}$) and the precursor (P3) annealed at different temperatures (600 $^\circ\text{C}$, 800 $^\circ\text{C}$, 1000 $^\circ\text{C}$ and 1200 $^\circ\text{C}$), respectively. In **Fig. 6a**, two broad peaks at 26.0°, 42.4° (θ) can be indexed to the (002) and (100) interlayers reflection of h-BCN (ICDD card 35–1292) and the broad peak at around 21° could be ascribed to amorphous phases suggesting insufficient pyrolyzation and crystallization of the precursors at relatively lower temperature. Additionally, it can be clearly seen that the intensities of the (002) and (100) diffraction peaks rise up with the increase of ethylenediamine contents. **Fig. 6b** shows a group of XRD patterns of the as-prepared h-BCN bulks annealed at 600, 800, 1000 and 1200 $^\circ\text{C}$ with P3, respectively. The diffraction peaks (θ) at 26.0°, 42.4°, 54.0° and 77.5° can be indexed to the (002), (100), (004) and (110) planes of h-BCN (ICDD card 35–1292), respectively. Moreover, with the increase of the annealing temperatures, the intensities of these characteristic peaks become stronger and the full width half maximum (FWHM) become narrower. The diffraction peak at higher θ (77.5°) gradually emerges with the temperature elevating. The broad peaks indicate the formation of nanosized domains and low correlation lengths according to Scherrer formula [26].

Raman spectra of the bulk h-BCN samples prepared from different types of precursors (P1, P2 and P3) at the same annealing temperature (500 $^\circ\text{C}$) are shown in **Fig. 6c**. **Fig. 6d** shows the Raman spectra of the sample P3 annealed at different temperatures (600, 800, 1000 and 1200 $^\circ\text{C}$). The two groups of spectra both in **Fig. 6c** and **d** shows the characteristic D and G bands approximately at 1344 and 1601 cm^{-1} . In **Fig. 6d**, the bulk h-BCN samples show D + D at 2690 cm^{-1} and D + G bands at 2910 cm^{-1} , indicating the graphitic structure. D bands of carbon related materials originate from the finite crystal size or lattice distortion which is associated with sp^3 defect sites, while the G bands are caused by stretching of all sp^2 pairs (B-C, B-N, C-C and B-N bonds) [52,53]. The D + D bands

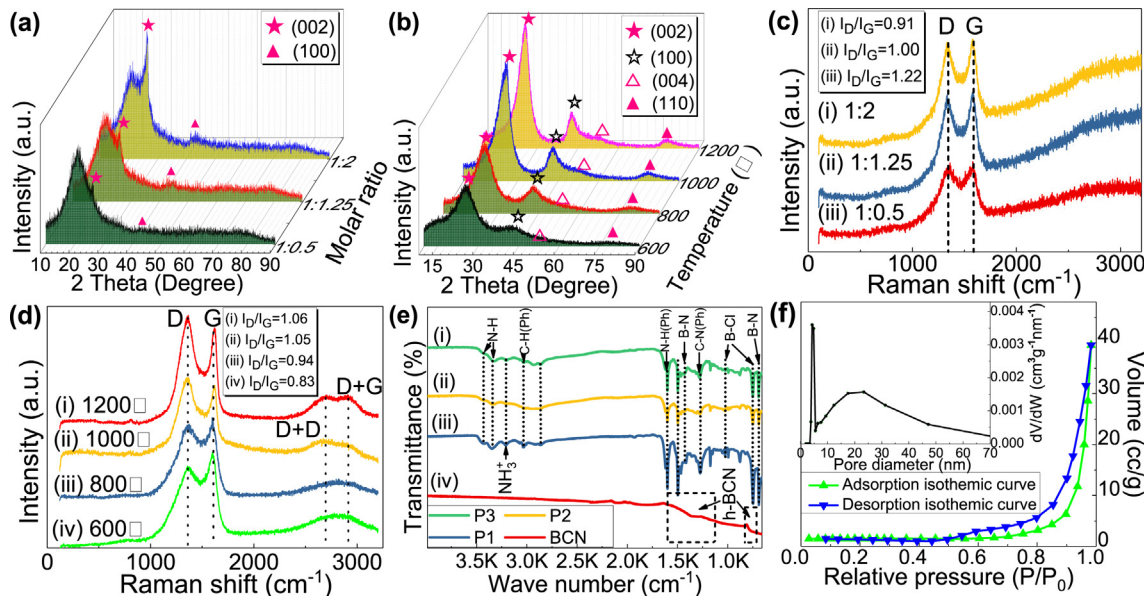


Fig. 6. - Evidence for the lattice structure, the status of layers, the chemical groups and the pore characteristics of h-BCN bulk. (a, b) XRD patterns and **(c, d)** Raman spectra of h-BCN samples from different types of precursors annealed at 500 °C **(a, c)** and from different annealing temperatures with P3 **(b, d)**, respectively. **(e)** The FT-IR spectra of h-BCN bulk and different types of precursors, respectively. **(f)** Nitrogen adsorption-desorption isotherm of h-BCN bulk and mesopore size distribution (inset).

has been used to indicate the quality and number of layers of graphene according to its relative intensity with respect to the G band and its position [54,55] suggesting that the h-BCN bulk is composed by numerous h-BCN layers, which agrees well with the results in Fig. 4 and Fig. S2 a–c. Obviously, in Fig. 6c, the observed I_D/I_G values decrease from 1.22 to 0.90 with the increasing molar ratios of ethylenediamine (from P1 to P3), indicating that the structural defects decrease in the edge plane and the formation of h-BCN nanoflakes become completer [56]. This phenomenon is consistent with the observed SEM results in Fig. 3. Similar trend is reported by Lee *et al.* that the I_D/I_G is from 1.0 for $B_{0.26}C_{0.57}N_{0.17}$ to 0.68 for $B_{0.11}C_{0.85}N_{0.44}$ [57]. In Fig. 6d, with the increasing of pyrolysis temperature, the I_D/I_G values increase from 0.83 to 1.06, which has the same rule in reported literature [22,58]. With the increase of pyrolysis temperature, more defects would form in the B-C-N lattice because the hybrid B and N atoms can distort the C-C networks. Furthermore, in Fig. 6d, the D + D and D + G bands gradually emerge and the intensity increase with the increasing temperature which further confirms the addition of B and N dopants in C-C networks.

Fig. 6e shows the FT-IR spectra for the h-BCN precursors (P1, P2 and P3) and h-BCN bulk. From Fig. 6e (i) to (iii), the typical peaks of the basic structures for the precursors (cm^{-1}): N-H (3428, 3350), Phenyl C-H (3037), Phenyl N-H (1600), Phenyl C-N (1275), and B-N (1417, 690), B-Cl (749) and NH_3^+ (3211) [59,60]. From P1 to P3, all the precursors have the same chemical bonds even though the molar ratio of ethylenediamine increases in sequence. Therefore, these typical peaks indicate that the synthesis process of precursors agrees well with Equation (1). Fig. 6e (iv) shows the FT-IR spectrum of the sintered product and the broad IR absorption bands at 1120–1600 cm^{-1} and 710–830 cm^{-1} correspond to the in-plane stretching vibrations and out-of-plane bending modes within the $\text{B}_x\text{C}_y\text{N}_z$ heterocycles, respectively. R. Gago *et al.* has reported that the ternary BCN compound would show a little shoulder at 1200 cm^{-1} with an obvious absorption peak around 1300–1400 cm^{-1} [61–64]. Therefore, the absorption peak at 1363 cm^{-1} in Fig. 6e (iv) could be the typical band from the ternary h-BCN compound.

Nitrogen adsorption-desorption isotherms (Fig. 6f), obtained at 77 K, strictly fall within the IUPAC classification group as type-III and the curves exhibit a hysteresis loop (type H3) in the relative pressure region (P/P_0) of 0.45–1.0 [65]. The sorption isotherms indicate that the multilayer, associated with non-rigid aggregates of plate-like particles giving rise to slit-shaped pores, exists in h-BCN bulk corresponding to the observed structure in SEM and TEM (Figs. 3 and 4 and Fig. S2). The pore size distribution (PSD, inset of Fig. 6f), obtained by the Barrett-Joyner-Halenda (BJH) method, calculated from recorded adsorption isotherms, reveals that most of the pore volume is contributed by mesoporous whose diameter is less than 10 nm (mainly around 5 nm) and the distribution range is approximately from 10 to 50 nm. The prominent pores size distribution ranges from 4 to 6 nm, implying the existence of narrow mesoporous in the h-BCN nanosheets.

As can be seen in Fig. 7, the thermal stability for the h-BCN bulks synthesized at different temperatures (800, 1000 and 1200 °C) is investigated by thermogravimetric analysis (TGA) from room

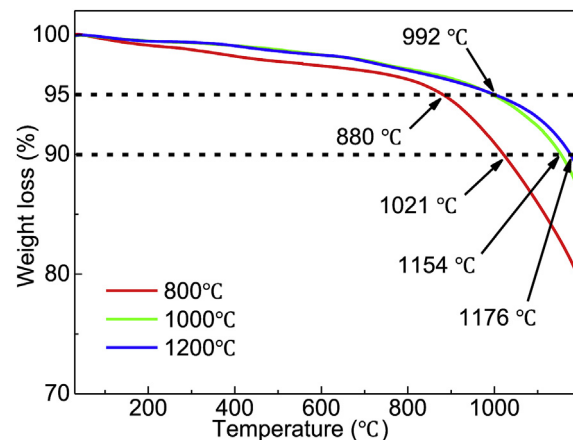


Fig. 7. The thermal stability of h-BCN bulk prepared at different temperature: TGA profiles measured in N_2 .

temperature (25°C) to 1200°C . The couple curves for the samples prepared at 1000 and 1200°C almost overlap till 992°C , implying the similar thermal stability below 1000°C and the weight loss at 992°C are only 5%. The total weight loss at 1200°C for the samples prepared at 1000 and 1200°C is 12.5, 10.8%, respectively. While, for the sample annealed at 800°C , the weight loss is 19.8% at 1200°C , which is larger than the former. These phenomena indicate that the thermostability of h-BCN bulk increases with the increasing pyrolysis temperature and it could be explained by the fact that nanocrystallines in the h-BCN would stabilize the structure.

Fig. 8a-d shows the X-ray photoelectron spectroscopy (XPS) spectrum of BCN and high resolution spectra of B, N and C, respectively, to further investigate the elemental composition and chemical structure of as-prepared h-BCN. The shape and position of the spectra of all three elements are obviously divergent from those of previous BCN ternary composition [66,67]. **Fig. 8a** shows the existence of B, C, N and O elements for the sample, from which the chemical composition is around $\text{B}_{0.05}\text{C}_{0.09}\text{N}_{0.86}$. The O peak at around 531 eV is due to the physical absorption of H_2O on the surface due to the mesoporous structure [22]. **Fig. 8b** shows the B 1s spectrum of as-prepared h-BCN bulk. The peak is located at 190.3 eV which is very close to the location of B 1s in h-BN [52,68]. The band has been deconvoluted to three bands at 180.6, 190.3, and 191.1 eV, assigned to B-C, B-N, B-O, respectively (**Fig. 8b**) where the amount of B bonded to N is higher than C or O species from the intensities of these three bands. The binding energy of the B atoms would be expected to follow the order $\text{B}-\text{C} < \text{B}-\text{N} < \text{B}-\text{O}$, due to the electronegativity differences between the four atoms $\text{B} < \text{C} < \text{N} < \text{O}$ [52,69–73]. Based on the same principle of electronegativity differences and the existence of the shoulders on the other two spectra in **Fig. 8c** and d, then **Fig. 8c** can be deconvoluted to three bands at 283.7, 285.0, 286.8 eV which can be assigned to C-B, C-C and C-N, respectively, where the percentage of C bonded to B is higher than C or N from the intensities of these three band as well. The C-N bonding energy is higher than our previous report [39] and others' reports [74] which could be explained that the other

configurations, presented as dangling bonds, such as $\text{C}=\text{O}$ or $\text{C}\equiv\text{N}$, are included. As for **Fig. 8d**, the spectrum shows N 1s of the h-BCN which can be divided to 398.4, 399.2, 401.0 eV attributed to N-B, N-C and N-C bonds, respectively. The two N-C bonds can demonstrate that two different band structures exist in h-BCN where the lower energy N-C bond with relative higher intensity shows graphite-like N-C structures and the higher energy one shows the N atoms bonded to C atoms as pyridine-like structures indicating that the amount of graphitic N is relative larger than the pyridinic N [75,76].

3.3. Electromagnetic parameters and microwave absorption properties of h-BCN bulks and h-BCN MTs

A schematic representation for the possible dissipation route in h-BCN bulk is shown in **Fig. 9a**. The absorption mechanisms including multiple dissipations (induced currents, impedance matching) for incident EMW would coexist to dissipate electromagnetic energy due to the multiple interfaces (hybrid B-C-N networks with abundant mesopores in the structures). On one hand, in incident electromagnetic field, the incident EMW will induce currents with finite electric conductivity in the h-BCN sheets and mesoporous and dissipated in forms of thermal energy [77]. And this process allows a sufficient absorption for EMW within the mesoporous structure. On the other hand, according to the previous calculation and simulation by the first principle (**Fig. 1**), h-BCN exists electronic polarization or interfacial polarization associated with lattice relaxation which can simultaneously contribute to the dielectric loss. Moreover, electron migration would exist inside h-BCN bulk when exposed to electromagnetic field, which leads to electric charge accumulation at the disorder interfaces and defects, acting as a “micro-capacitor”. And this would attribute to the improved impedance matching. Theoretically, the designed h-BCN could have a pretty good performance in EMW absorption.

In order to visually observe the promising absorption performance, the EMW absorption properties (RL values) are shown with

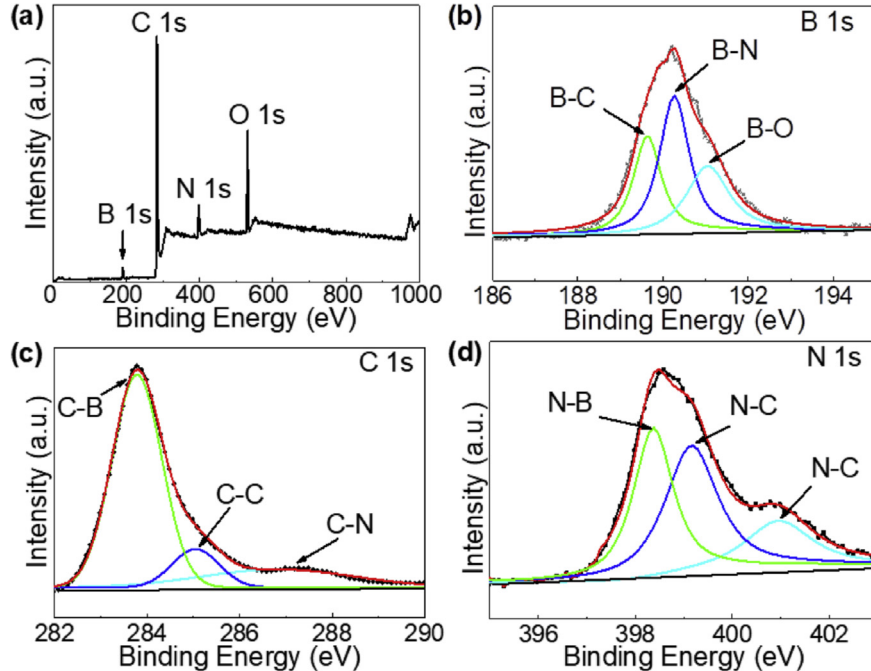


Fig. 8. Evidence for the chemical bonds and composition of h-BCN bulk. (a) XPS spectrum of h-BCN. (b)–(d) XPS spectra of B, C and N 1s core levels respectively. The spectrum curves (filled diamonds) are deconvoluted (colorful solid curves) by Gaussian fitting (red curve).

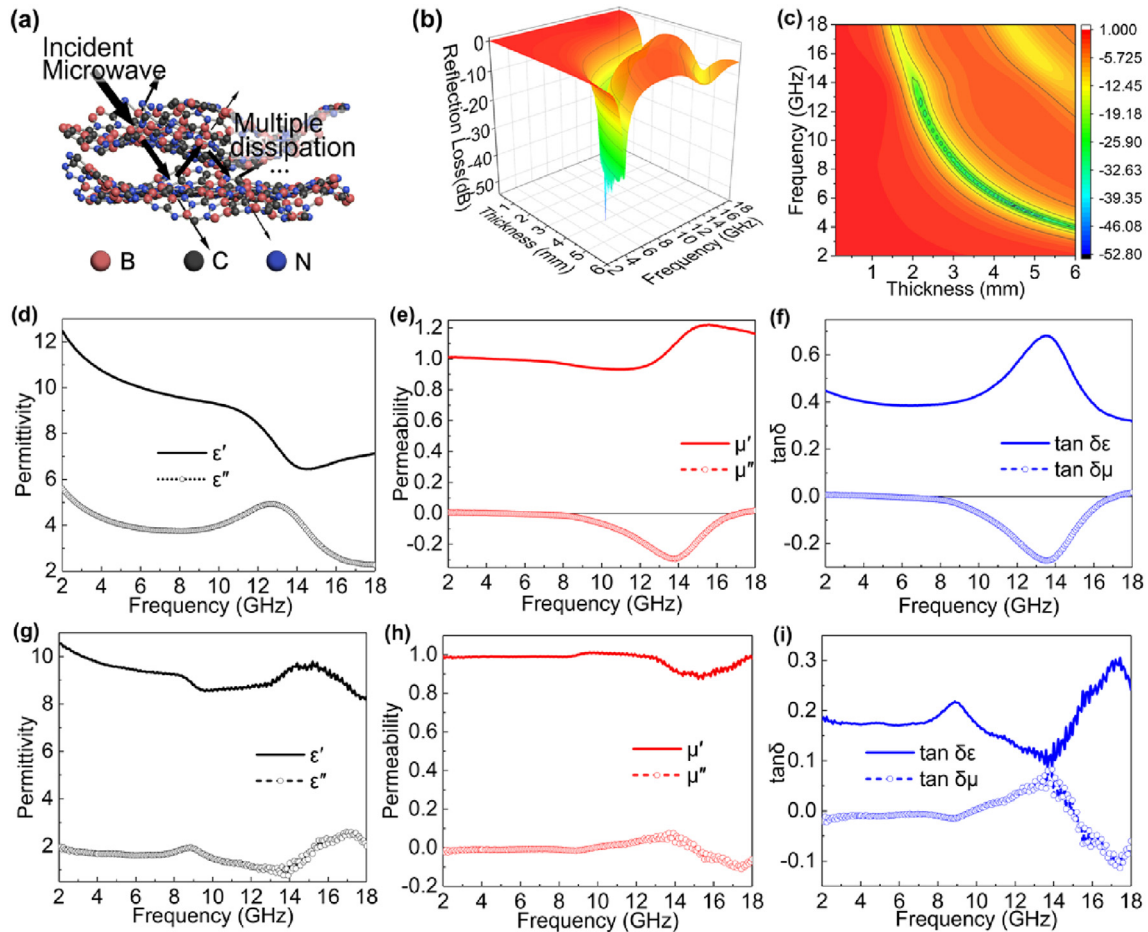


Fig. 9. The mechanism and performances of EMW absorption for h-BCN bulk. (a) A schematic representation for the possible dissipation route of EMW in h-BCN networks. (b–f) Showing the related electromagnetic parameters and EMW absorption properties of h-BCN bulks, annealed by H3 heating mode with P3 precursor: (b) the 3D colormapped wireframe surface of the RL values with different thickness and frequency, (c) a contour revealing the best performance for practical application, (d–f) frequency dependence of the complex relative permittivity, complex relative permeability, dielectric loss and magnetic loss tangent, respectively. (g–i) Showing the related electromagnetic parameters of h-BCN bulks, annealed by H3 heating mode with P2 precursor: (g–i) frequency dependence of the complex relative permittivity, complex relative permeability, dielectric loss and magnetic loss tangent, respectively.

the frequency and thickness in Fig. 9b and c by a 3D colormapped wireframe surface and a contour, respectively. To measure the EMW absorbing properties of the as-prepared h-BCN bulk, paraffin composites incorporated with 20 wt% h-BCN powder (originated from P3 precursor) were prepared for the electromagnetic parameters (Fig. 9d–f). The complex relative permittivity ($\epsilon_r = \epsilon' - j\epsilon''$) and complex relative permeability ($\mu_r = \mu' - j\mu''$), whose real parts (ϵ', μ') and imaginary parts (ϵ'', μ'') represent the energy storage and dissipation capability, respectively, were measured by the transmission/refection coaxial line method [43,78,79]. The real part of the complex permittivity (Fig. 9d) has an obvious decrease from 2 to 18 GHz but has the character of one knee at around 11 GHz on the curve. This characteristic could improve the impedance matching for the EMW absorber [80]. The imaginary part of the complex permittivity has two conspicuous resonance peaks from 2 to 18 GHz. The resonance caused by vacancies or pores in h-BCN sheets usually dominates the low-frequency range and the high-frequency resonance can be explained by electronic polarization which agrees well with the aforementioned calculation and analysis [81,82].

The complex relative permeability parameters are shown in Fig. 9e. Because of h-BCN has no magnetic features, it is interesting that the imaginary part (μ'') of the complex permeability shows the

negative value from 4.72 to 17.12 GHz and the minimum value is –0.27 at 13.68 GHz. Many tests have been carried out to avoid error results but they all show quite similar negative μ'' . According to the reports, the left-hand materials have both negative permittivity and permeability [83]. However, this uncommon phenomenon cannot be attributed to left-hand materials and because of the reported study in which the multi-walled CNT/paraffin composites had negative permeability explained as the magnetic energy is radiated out from the CNT composites [81]. Hence, the more detailed mechanism needs further study. In Fig. 9f, the measured dielectric loss factor ($\tan \delta_\epsilon = \epsilon''/\epsilon'$) and magnetic loss factor ($\tan \delta_\mu = \mu''/\mu'$) vary from 0.318 to 0.681 and from –0.272 to 0.017, respectively. In addition, both dielectric and magnetic loss can determine the intrinsic microwave absorption. The $\tan \delta_\epsilon$ is obviously far larger than the $\tan \delta_\mu$, revealing that the intrinsic EMW absorption of h-BCN bulk mainly depends on the dielectric performance.

On the basis of the previously measured EMW parameters (Fig. 9d–f), reflection loss (RL) of the samples can be obtained through calculation and simulation. The impedance of Z_0 can be figured out by Equation (3) when EMW travel through free space. The input impedance Z_{in} , when the EMW transmission happens on the medium surface, can be described by Equation (4) [43,84]. According to transmission line theory, the RL (dB), on the absorber

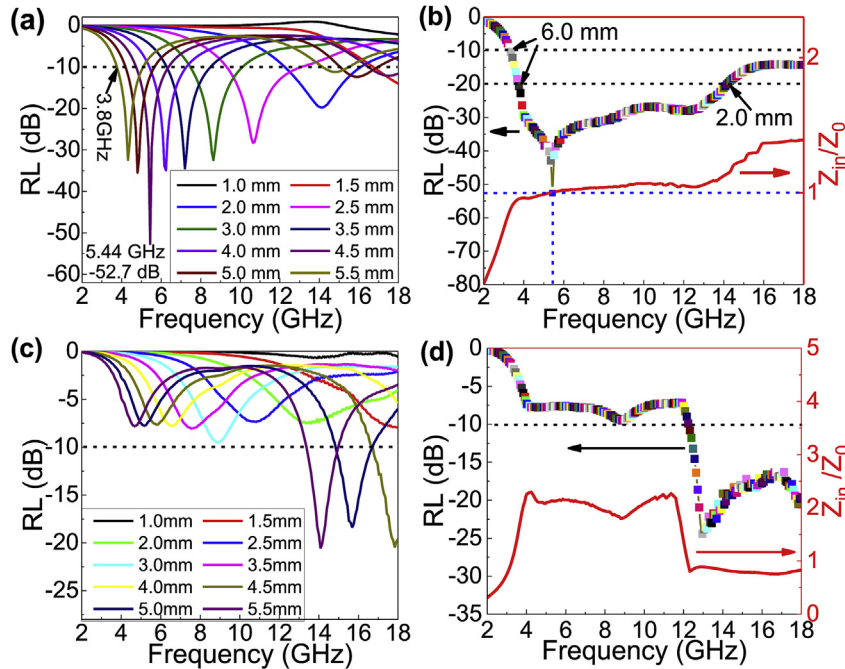


Fig. 10. RL curves and RL peak values and normalized input impedance dependence of RL peak frequency of h-BCN bulks: (a, b) annealed by H3 heating mode with P3 precursor, (c, d) annealed by H3 heating mode with P2 precursor.

surface, can be calculated and simulated by Equation (5) for a single-layer absorbing material backed by a perfect conductor [43,85,86]. The three equations are given as follows:

$$Z_0 = \sqrt{\frac{\mu_0}{\epsilon_0}} \quad (3)$$

$$Z_{in} = Z_0 \sqrt{\frac{\mu_r}{\epsilon_r}} \tanh \left[j \frac{2\pi f d}{c} \sqrt{\mu_r \epsilon_r} \right] \quad (4)$$

$$RL = 20 \log \left| \frac{Z_{in} - Z_0}{Z_{in} + Z_0} \right| \quad (5)$$

where μ_0 is the complex relative permeability, ϵ_0 is permittivity of free space, μ_r is the complex relative magnetic permeability and ϵ_r is the dielectric permittivity, f is the frequency of EMW, d is the thickness of an absorber, and c is the velocity of EMW in free space.

Fig. 9g–i shows the electromagnetic parameters performance of h-BCN bulk originated from P2 precursor, which are quite different with the former sample which is originated from P3 precursor except that the two samples both have the negative imaginary parts of permeability (Fig. 9h) and both the dielectric loss dominate the EMW absorption (Fig. 9g). In Fig. S3 a and b, semicircles could be observed and the centers of these circles lie above the real axis which suggests the dual dielectric relaxation processes deviating from Debye type in h-BCN/wax [87]. Due to the electronic accumulation on the surfaces of hybrid B-C-N networks with abundant mesopores in the structures as well as on the defects inside the bulk structure under external electric field, the disorder or defects insides materials could act as a “micro-capacitor” and promote dielectric permittivity [88]. Therefore, this tunable EMW absorbing properties of the h-BCN bulk are mainly attributed to the improved impedance matching as well as dissipation resulted from hopping migration. In Fig. 9d and g, Fig. 9d shows that the h-BCN bulk ceramic originated from P3 precursor has larger both the real and imaginary parts of complex permittivity than the one originated

from P2 precursor, suggesting that the h-BCN bulk ceramic originated from P3 precursor have higher electric conductivity than that from P2 precursor, which agrees well with the simulation results, indicating that the tunability exists in permittivity as well.

Fig. 10a shows the RL curves at the sample thickness from 1.0 to 5.5 mm. The RL peak appears at a frequency when the thickness was given. According to Equation (5), when the reflectivity of a material is smaller than -10 dB, it means that the h-BCN samples have the ability to absorb 90% of EMW energy. Therefore, the RL value below -10 dB can be a critical characterization for the effective absorption of EMW [89]. If the reflection value is below -20 dB, the EMW absorption with the percentage of absorption as high as 99% suggests that the tested materials could be an excellent absorber [26]. Apparently, in Fig. 10a, the RL values totally exceed -10 dB from 3.8 to 18.0 GHz (the maximum is 18 GHz in our equipment) with a thickness of 1.5–5.5 mm and the RL values below -20 dB are showed from 4.1 to 11.2 GHz with the thickness of 2.5–5.5 mm, indicating that the h-BCN bulk has an excellent capability to efficiently absorb EMW in a wide frequency range. Additionally, the minimum value of RL -52.7 dB was observed at 5.44 GHz with the thickness of 4.5 mm, which means a nearly complete absorption. According to the reported carbonaceous absorbers, Fe/C shows a minimum RL -34 dB at 9.6 GHz [90] and the boron incorporated architectures present the minimum RL -33.6 dB at 15.28 GHz [26]. Fig. 10b shows the recorded RL peak values at every given absorber thickness and the normalized input impedance (Z_{in}/Z_0). The curve of RL peak values shows a rapid decrease to the lowest value -52.7 dB at 5.44 GHz (the value of Z_{in}/Z_0 is just nicely equals to 1 at the perfect matching point), and then increases gradually with a zig-zag route. Moreover, the RL peak values below -10 dB is from 3.36 to 18 GHz with the thickness below 6.0 mm and below -20 dB is from 3.78 to 14.16 GHz with the thickness from 6.0 to 2.0 mm, respectively. The results indicate that the h-BCN bulk has an excellent absorption performance from S band (2–4 GHz) to Ku band (12–18 GHz).

The RL curves of h-BCN bulk originated from P2 precursor at the

thickness from 1.0 mm to 5.5 mm and the RL peak values with normalized impedance are shown in Fig. 10c and d, respectively. Fig. 10c shows that the RL below –10 dB from 13.4 to 18.0 GHz with the thickness below 5.5 mm. The minimum RL value is –20.6 dB at 14.8 GHz with the thickness of 5.5 mm. In Fig. 10d, the curve of Z_{in}/Z_0 has no intersection with the RL peak curve revealing the incomplete impedance matching. This kind of h-BCN bulk shows a relatively good performance of EMW absorption at high frequency. In comparison, the former h-BCN bulk (Fig. 10a–b) has a better performance in EMW absorption with a broader range and lower RL value. The difference between these two h-BCN bulks is only the precursor type that the former has the higher ratio of ethylenediamine. The higher N dopants introduced in B-C-N networks would improve the EMW absorption property according to the RL measurements. Therefore, the EMW absorption performance of h-BCN can be tuned by changing the ratio of N dopants which is in accordance with the theoretical prediction by the first principle. Additionally, the EMW absorption properties of h-BCN MTs annealed by H3 heating mode with precursor P3 are also studied in Fig. S4. The electromagnetic parameters are shown in Fig. S4 a. The curve profiles are similar to that of h-BCN bulk synthesized by P2 precursor. The imaginary parts of permeability of h-BCN MTs also have a typical negative value with a resonance peak at ~17 GHz, which could be an inherent attribute of h-BCN materials. Fig. S4 b show that the h-BCN MTs have a poor performance of EMW absorption with all the RL values above –10 dB from 2 to 18 GHz because of the lower surface area (thinner hollow chambers) for this product according to TEM results (Fig. S2 g). The minimum RL value –8.2 dB at 17.9 GHz at the sample thickness of 1.0 mm is observed from Fig. S4 b due to the unmatched impedance Z_{in}/Z_0 (weak resonance absorption). Moreover, from the EDS spectrum in Fig. S1 d and the EDS-mapping of a segment of microtube (Fig. S2 j–l), the N concentration of the h-BCN MTs is comparatively lower than the h-BCN bulk, indicating that the ratio of N dopants in B-C-N networks could impact on the EMW absorption (weak polarization effects).

4. Conclusions

The h-BCN architectures of ultra-light h-BCN bulk and h-BCN MTs are simultaneously synthesized by pyrolysis of a simple precursors in a tube furnace. The polymerization mechanism of the h-BCN precursors, lattice and density of electron features, pyrolysis processes, morphologies with different structures, and the EMW absorption properties were systematically studied. The h-BCN bulk exhibits a considerable low density of 15 mg/cm³ with the controllable EMW absorption from the minimum RL –52.7 dB at 5.44 GHz to –20.6 dB at 14.8 GHz just by changing the reacting monomers. The EMW absorption bands (from S to Ku) can be designed guided by the first principle calculation. The products also have an outstanding thermal stability (the weight loss is only 10.8% at 1200 °C) which could be a candidate for next generation stealth materials (especially critical Mach number aircraft) and industrial shielding materials.

Acknowledgment

This work was supported by National Natural Science Foundation of China (51302049), Project of Natural Scientific Research Innovation Foundation in Harbin Institute of Technology (HIT.NSRIF.2015106, HIT.NSRIF.2014129), Technology Development Program at Weihai (2013DXGJ12), the National Nature Science Foundation of China (Grant No. 91326102) and Project of the Field of Equipment Development (61409220111).

Appendix A. Supplementary data

Supplementary data related to this article can be found at <https://doi.org/10.1016/j.carbon.2018.05.001>.

Author contributions

§ Tao Zhang and Jian Zhang contributed equally to this work.

References

- [1] Y. Zhang, Y. Huang, T. Zhang, H. Chang, P. Xiao, H. Chen, et al., Broadband and tunable high-performance microwave absorption of an ultralight and highly compressible graphene foam, *Adv. Mater.* 27 (12) (2015) 2049–2053.
- [2] P. Liu, Y. Huang, Y. Yang, J. Yan, X. Zhang, Sandwich structures of graphene@Fe 3 O 4 @PANI decorated with TiO 2 nanosheets for enhanced electromagnetic wave absorption properties, *J. Alloy. Compd.* 662 (2016) 63–68.
- [3] T.-Y. Wu, K.-T. Lu, C.-H. Peng, Y.-S. Hong, C.-C. Hwang, A new method for the preparation of a Fe3O4/graphene hybrid material and its applications in electromagnetic wave absorption, *Mater. Res. Bull.* 70 (2015) 486–493.
- [4] D. Sun, Q. Zou, G. Qian, C. Sun, W. Jiang, F. Li, Controlled synthesis of porous Fe3O4-decorated graphene with extraordinary electromagnetic wave absorption properties, *Acta Materialia* 61 (15) (2013) 5829–5834.
- [5] Y. Chen, H.-B. Zhang, Y. Yang, M. Wang, A. Cao, Z.-Z. Yu, High-performance epoxy nanocomposites reinforced with three-dimensional carbon nanotube sponge for electromagnetic interference shielding, *Adv. Funct. Mater.* 26 (3) (2016) 447–455.
- [6] Y. Qing, X. Wang, Y. Zhou, Z. Huang, F. Luo, W. Zhou, Enhanced microwave absorption of multi-walled carbon nanotubes/epoxy composites incorporated with ceramic particles, *Compos. Sci. Technol.* 102 (2014) 161–168.
- [7] T. Zhang, B. Xiao, P. Zhou, L. Xia, G. Wen, H. Zhang, Porous-carbon-nanotube decorated carbon nanofibers with effective microwave absorption properties, *Nanotechnology* 28 (35) (2017) 355708.
- [8] G. Li, T. Xie, S. Yang, J. Jin, J. Jiang, Microwave absorption enhancement of porous carbon fibers compared with carbon nanofibers, *J. Phys. Chem. C* 116 (16) (2012) 9196–9201.
- [9] G. Wang, Z. Gao, S. Tang, C. Chen, F. Duan, S. Zhao, et al., Microwave absorption properties of carbon nanocoils coated with highly controlled magnetic materials by atomic layer deposition, *ACS Nano* 6 (12) (2012) 11009–11017.
- [10] L. Wang, Y. Guan, X. Qiu, H. Zhu, S. Pan, M. Yu, et al., Efficient ferrite/Co/porous carbon microwave absorbing material based on ferrite@metal–organic framework, *Chem. Eng. J.* 326 (2017) 945–955.
- [11] Q. Liu, B. Cao, C. Feng, W. Zhang, S. Zhu, D. Zhang, High permittivity and microwave absorption of porous graphitic carbons encapsulating Fe nanoparticles, *Compos. Sci. Technol.* 72 (13) (2012) 1632–1636.
- [12] Y. Huang, Y. Wang, Z. Li, Z. Yang, C. Shen, C. He, Effect of pore morphology on the dielectric properties of porous carbons for microwave absorption applications, *J. Phys. Chem. C* 118 (45) (2014) 26027–26032.
- [13] Q. Liu, D. Zhang, T. Fan, Electromagnetic wave absorption properties of porous carbon/Co nanocomposites, *Appl. Phys. Lett.* (1) (2008) 93, 013110.
- [14] S.-Y. Tong, M.-J. Tung, W.-S. Ko, Y.-T. Huang, Y.-P. Wang, L.-C. Wang, et al., Effect of Ni fillers on microwave absorption and effective permeability of NiCuZn ferrite/Ni/polymer functional composites, *J. Alloy. Compd.* 550 (2013) 39–45.
- [15] T. Wang, Z. Liu, M. Lu, B. Wen, Q. Ouyang, Y. Chen, et al., Graphene–Fe3O4 nanohybrids: synthesis and excellent electromagnetic absorption properties, *J. Appl. Phys.* (2) (2013) 113, 024314.
- [16] S.C. Chiu, H.C. Yu, Y.Y. Li, High electromagnetic wave absorption performance of silicon carbide nanowires in the Gigahertz range, *J. Phys. Chem. C* 114 (4) (2010) 1947–1952.
- [17] R. Wu, K. Zhou, Z. Yang, X. Qian, J. Wei, L. Liu, et al., Molten-salt-mediated synthesis of SiC nanowires for microwave absorption applications, *CrysEngComm* 15 (3) (2013) 570–576.
- [18] W. Duan, X. Yin, Q. Li, X. Liu, L. Cheng, L. Zhang, Synthesis and microwave absorption properties of SiC nanowires reinforced SiOC ceramic, *J. Eur. Ceram. Soc.* 34 (2) (2014) 257–266.
- [19] Y. Hou, L. Cheng, Y. Zhang, Y. Yang, C. Deng, Z. Yang, et al., Electrospinning of Fe/SiC hybrid fibers for highly efficient microwave absorption, *ACS Appl. Mater. Interfaces* 9 (8) (2017) 7265–7271.
- [20] Q. Wen, Y. Feng, Z. Yu, D.-L. Peng, N. Nicoloso, E. Ionescu, et al., Microwave absorption of SiC/HfCxN1–x/C ceramic nanocomposites with HfCxN1–x–carbon core-shell particles, *J. Am. Ceram. Soc.* 99 (8) (2016) 2655–2663.
- [21] F. Ye, L. Zhang, X. Yin, Y. Liu, L. Cheng, The improvement of wave-absorbing ability of silicon carbide fibers by depositing boron nitride coating, *Appl. Surf. Sci.* 270 (2013) 611–616.
- [22] E. Iyyamperumal, S. Wang, L. Dai, Vertically aligned BCN nanotubes with high capacitance, *ACS Nano* 6 (6) (2012) 5259–5265.
- [23] X.D. Bai, E.G. Wang, J. Yu, H. Yang, Blue-violet photoluminescence from large-scale highly aligned boron carbonitride nanofibers, *Appl. Phys. Lett.* 77 (1) (2000) 67–69.
- [24] X. Blase, J.C. Charlier, A. DeVita, R. Car, Theory of composite BxCyNz nanotube

- heterojunctions, *Appl. Phys. Lett.* 70 (2) (1997) 197–199.
- [25] Y. Miyamoto, A. Rubio, M.L. Cohen, S.G. Louie, Chiral tubules of hexagonal B₂N, *Phys. Rev. B* 50 (7) (1994) 4976–4979.
- [26] Y. Kang, Z. Chu, D. Zhang, G. Li, Z. Jiang, H. Cheng, et al., Incorporate boron and nitrogen into graphene to make BCN hybrid nanosheets with enhanced microwave absorbing properties, *Carbon* 61 (2013) 200–208.
- [27] T. Wang, H. Wang, X. Chi, R. Li, J. Wang, Synthesis and microwave absorption properties of Fe–C nanofibers by electrospinning with disperse Fe nanoparticles parceled by carbon, *Carbon* 74 (8) (2014) 312–318.
- [28] M. Terrones, A.M. Benito, C. MantecaDiego, W.K. Hsu, O.I. Osman, J.P. Hare, et al., Pyrolytically grown BxCyNz nanomaterials: nanofibres and nanotubes, *Chem. Phys. Lett.* 257 (5–6) (1996) 576–582.
- [29] Y. Zhang, H. Gu, K. Suenaga, S. Iijima, Heterogeneous growth of B–C–N nanotubes by laser ablation, *Chem. Phys. Lett.* 279 (5–6) (1997) 264–269.
- [30] J. Yu, J. Ahn, S.F. Yoon, Q. Zhang, Gan B. Rusli, et al., Semiconducting boron carbonitride nanostructures: nanotubes and nanofibers, *Appl. Phys. Lett.* 77 (13) (2000) 1949–1951.
- [31] C.Y. Zhi, J.D. Guo, X.D. Bai, E.G. Wang, Adjustable boron carbonitride nanotubes, *J. Appl. Phys.* 91 (8) (2002) 5325–5333.
- [32] S. Enouz-Vedrenne, O. Stephan, M. Glerup, J.L. Cochon, C. Colliex, A. Loiseau, Effect of the synthesis method on the distribution of C, B, and N Elements in multiwall nanotubes: a spatially resolved electron energy loss spectroscopy study, *J. Phys. Chem. C* 112 (42) (2008) 16422–16430.
- [33] F. Piazza, J.E. Nocua, A. Hidalgo, J. De Jesus, R. Velazquez, B.L. Weiss, et al., Formation of boron carbonitride nanotubes from *in situ* grown carbon nanotubes, *Diam. Relat. Mater.* 14 (3–7) (2005) 965–969.
- [34] L. Wang, Y. Huang, C. Li, J. Chen, X. Sun, A facile one-pot method to synthesize a three-dimensional graphene@carbon nanotube composite as a high-efficiency microwave absorber, *Phys. Chem. Chem. Phys. PCCP* 17 (3) (2015) 2228–2234.
- [35] H.-M. Xiao, X.-M. Liu, S.-Y. Fu, Synthesis, magnetic and microwave absorbing properties of core-shell structured MnFe2O4/TiO2 nanocomposites, *Compos. Sci. Technol.* 66 (13) (2006) 2003–2008.
- [36] F. Xia, J. Liu, D. Gu, P. Zhao, J. Zhang, R. Che, Microwave absorption enhancement and electron microscopy characterization of BaTiO3 nano-torus, *Nanoscale* 3 (9) (2011) 3860.
- [37] D.X. Li, D.L. Yu, B. Xu, J.L. He, Z.Y. Liu, P. Wang, et al., Synthesis of semimetallic BC₃N with orthorhombic structure at high pressure and temperature, *Cryst. Growth Des.* 8 (7) (2008) 2096–2100.
- [38] T. Zhang, G. Wen, Y.P. Wang, L. Xia, Monodispersed boron carbonitride hollow spheres with high-performance microwave absorption property, *Mater. Res. Bull.* 74 (2016) 177–181.
- [39] T. Zhang, S. Zeng, G. Wen, J. Yang, Novel carbon nanofibers build boron carbonitride porous architectures with microwave absorption properties, *Microporous Mesoporous Mater.* 211 (2015) 142–146.
- [40] D. Trivedi, H. Nalwa, *Handbook of Organic Conductive Molecules and Polymers*, vol. 2, Wiley, Chichester, 1997, pp. 505–572.
- [41] V. Denysenkov, M. Terekhov, R. Maeder, S. Fischer, S. Zangos, T. Vogl, et al., Continuous-flow DNP polarizer for MRI applications at 1.5 T, *Sci. Rep.* 7 (2017) 44010.
- [42] I. Stasinopoulos, S. Weichselbaumer, A. Bauer, J. Waizner, H. Berger, M. Garst, et al., Linearly polarized GHz magnetization dynamics of spin helix modes in the ferrimagnetic insulator Cu₂OSeO₃, *Sci. Rep.* 7 (1) (2017) 7037.
- [43] D. Zhang, Z. Hao, Y. Qian, Y. Huang, Yang Z. Bizeeng, et al., Simulation and measurement of optimized microwave reflectivity for carbon nanotube absorber by controlling electromagnetic factors, *Sci. Rep.* 7 (1) (2017) 479.
- [44] V.A. Dmitriev, M.G. Spencer, Chapter 2 SiC fabrication Technology: growth and doping, in: P. Yoon Soo (Ed.), *Semiconductors and Semimetals*, vol. 52, Elsevier, 1998, pp. 21–75.
- [45] R.J. Trew, Chapter 6 SiC microwave devices, in: P. Yoon Soo (Ed.), *Semiconductors and Semimetals*, vol. 52, Elsevier, 1998, pp. 237–282.
- [46] X. Ji, K. Jie, S.C. Zimmerman, F. Huang, A double supramolecular crosslinked polymer gel exhibiting macroscale expansion and contraction behavior and multistimuli responsiveness, *Polym. Chem.* 6 (11) (2015) 1912–1917.
- [47] K.H. Kim, Y. Oh, M.F. Islam, Graphene coating makes carbon nanotube aerogels superelastic and resistant to fatigue, *Nat. Nanotechnol.* 7 (9) (2012) 562–566.
- [48] G. Lian, X. Zhang, M. Tan, S. Zhang, D. Cui, Q. Wang, Facile synthesis of 3D boron nitride nanoflowers composed of vertically aligned nanoflakes and fabrication of graphene-like BN by exfoliation, *J. Mater. Chem.* 21 (25) (2011) 9201.
- [49] S.N. Mohammad, Thermodynamic imbalance, surface energy, and segregation reveal the true origin of nanotube synthesis, *Adv. Mater.* 24 (9) (2012) 1262–1275.
- [50] J. Fang, I. Levchenko, S. Kumar, D. Seo, K.K. Ostrikov, Vertically-aligned graphene flakes on nanoporous templates: morphology, thickness, and defect level control by pre-treatment, *Sci. Technol. Adv. Mater.* (5) (2014) 15, 055009.
- [51] K.S. Kim, Y. Zhao, H. Jang, S.Y. Lee, J.M. Kim, K.S. Kim, et al., Large-scale pattern growth of graphene films for stretchable transparent electrodes, *Nature* 457 (7230) (2009) 706–710.
- [52] L. Ci, L. Song, C. Jin, D. Jariwala, D. Wu, Y. Li, et al., Atomic layers of hybridized boron nitride and graphene domains, *Nat. Mater.* 9 (5) (2010) 430–435.
- [53] M.A. Pimenta, G. Dresselhaus, M.S. Dresselhaus, L.G. Cançado, A. Jorio, R. Saito, Studying disorder in graphite-based systems by Raman spectroscopy, *Phys. Chem. Chem. Phys. PCCP* 9 (11) (2007) 1276.
- [54] X. Li, W. Cai, J. An, S. Kim, J. Nah, D. Yang, et al., Large-area synthesis of high-quality and uniform graphene films on copper foils, *Science* 324 (5932) (2009) 1312.
- [55] A. Reina, X. Jia, J. Ho, D. Nezich, H. Son, V. Bulovic, et al., Large area, few-layer graphene films on arbitrary substrates by chemical vapor deposition, *Nano Lett.* 9 (1) (2009) 30–35.
- [56] G. Katagiri, H. Ishida, A. Ishitani, Raman spectra of graphite edge planes, *Carbon* 26 (4) (1988) 565–571.
- [57] Y.T. Lee, J. Park, Y.S. Choi, H. Ryu, H.J. Lee, Temperature-dependent growth of vertically aligned carbon nanotubes in the range 800–1100 °C, *J. Phys. Chem. B* 106 (31) (2002) 7614–7618.
- [58] S. Yong Bae, H. Won Seo, J. Park, Y. Sang Choi, J. Chul Park, S. Young Lee, Boron nitride nanotubes synthesized in the temperature range 1000–1200 °C, *Chem. Phys. Lett.* 374 (5–6) (2003) 534–541.
- [59] Y. Zheng, Y. Jiao, L. Ge, M. Jaroniec, S.Z. Qiao, Two-step boron and nitrogen doping in graphene for enhanced synergistic catalysis, *Angewandte Chemie* 52 (11) (2013) 3110–3116.
- [60] N. Tripathi, M. Yamashita, T. Uchida, T. Akai, Observations on size confinement effect in B–C–N nanoparticles embedded in mesoporous silica channels, *Appl. Phys. Lett.* (1) (2014) 105, 014106.
- [61] T. Komatsu, Bulk synthesis and characterization of graphite-like B–C–N and B–C–N heterodiiamond compounds, *J. Mater. Chem.* 14 (2) (2004) 221–227.
- [62] Y. Wada, Y.K. Yap, M. Yoshimura, Y. Mori, T. Sasaki, The control of B N and B C bonds in BCN films synthesized using pulsed laser deposition, *Diam. Relat. Mater.* 9 (3–6) (2000) 620–624.
- [63] J.H. Kaufman, S. Metin, D.D. Saperstein, Symmetry breaking in nitrogen-doped amorphous carbon: infrared observation of the Raman-active G and D bands, *Phys. Rev. B* 39 (18) (1989) 13053–13060.
- [64] I. Caretti, I. Jiménez, J.M. Albella, BCN films with controlled composition obtained by the interaction between molecular beams of B and C with nitrogen ion beams, *Diam. Relat. Mater.* 12 (3–7) (2003) 1079–1083.
- [65] K.S.W. Sing, D.H. Everett, R.A.W. Haul, L. Moscou, R.A. Pierotti, et al., Reporting physisorption data for gas solid systems with special reference to the determination of surface-area and porosity (recommendations 1984), *Pure Appl. Chem.* 57 (4) (1985) 603–619.
- [66] M.O. Watanabe, S. Itoh, K. Mizushima, T. Sasaki, Bonding characterization of BCN thin films, *Appl. Phys. Lett.* 68 (21) (1996) 2962–2964.
- [67] K. Raidongia, A. Nag, K.P. Hembram, U.V. Waghmare, R. Datta, C. Rao, BCN: a graphene analogue with remarkable adsorptive properties, *Chem. A Eur. J.* 16 (1) (2010) 149–157.
- [68] M. Kawaguchi, T. Kawashima, T. Nakajima, Syntheses and structures of new graphite-like materials of composition BCN(H) and BC3N(H), *Chem. Mater.* 8 (6) (1996) 1197–1201.
- [69] V. Linss, S. Rodil, P. Reinke, M. Garnier, P. Oelhafen, U. Kreissig, et al., Bonding characteristics of DC magnetron sputtered B–C–N thin films investigated by Fourier-transformed infrared spectroscopy and X-ray photoelectron spectroscopy, *Thin Solid Films* 467 (1) (2004) 76–87.
- [70] G. Bejarano, J. Caicedo, E. Baca, P. Prieto, A. Balogh, S. Enders, Deposition of B 4 C/BCN/c-BN multilayered thin films by rf magnetron sputtering, *Thin Solid Films* 494 (1) (2006) 53–57.
- [71] F. Zhou, K. Adachi, K. Kato, Influence of deposition parameters on surface roughness and mechanical properties of boron carbon nitride coatings synthesized by ion beam assisted deposition, *Thin Solid Films* 497 (1) (2006) 210–217.
- [72] C. Morant, P. Prieto, J. Bareño, J. Sanz, E. Elizalde, Hard BC x N y thin films grown by dual ion beam sputtering, *Thin Solid Films* 515 (1) (2006) 207–211.
- [73] M.N. Uddin, I. Shimoyama, Y. Baba, T. Sekiguchi, M. Nagano, X-ray photoelectron spectroscopic observation on B–C–N hybrids synthesized by ion beam deposition of borazine, *J. Vac. Sci. Technol. A Vac. Surf. Films* 23 (3) (2005) 497–502.
- [74] S.Y. Kim, J. Park, H.C. Choi, J.P. Ahn, J.Q. Hou, H.S. Kang, X-ray photoelectron spectroscopy and first principles calculation of BCN nanotubes, *J. Am. Chem. Soc.* 129 (6) (2007) 1705–1716.
- [75] H.C. Choi, S.Y. Bae, W.-S. Jang, J. Park, H.J. Song, H.-J. Shin, et al., Release of N2 from the carbon nanotubes via high-temperature annealing, *J. Phys. Chem. B* 109 (5) (2005) 1683–1688.
- [76] H.C. Choi, J. Park, B. Kim, Distribution and structure of N atoms in multiwalled carbon nanotubes using variable-energy X-ray photoelectron spectroscopy, *J. Phys. Chem. B* 109 (10) (2005) 4333–4340.
- [77] D. Micheli, R.B. Morles, M. Marchetti, F. Moglie, V. Mariani Primiani, Broad-band electromagnetic characterization of carbon foam to metal contact, *Carbon* 68 (2014) 149–158.
- [78] A.N. Yusoff, M.H. Abdullah, S.H. Ahmad, S.F. Jusoh, A.A. Mansor, S.A.A. Hamid, Electromagnetic and absorption properties of some microwave absorbers, *J. Appl. Phys.* 92 (2) (2002) 876–882.
- [79] Y.K. Hong, C.Y. Lee, C.K. Jeong, D.E. Lee, K. Kim, J. Joo, Method and apparatus to measure electromagnetic interference shielding efficiency and its shielding characteristics in broadband frequency ranges, *Rev. Sci. Instrum.* 74 (2) (2003) 1098–1102.
- [80] J.H. Zhou, J.P. He, G.X. Li, T. Wang, D. Sun, X.C. Ding, et al., Direct incorporation of magnetic constituents within ordered mesoporous carbon-silica nanocomposites for highly efficient electromagnetic wave absorbers, *J. Phys. Chem. C* 114 (17) (2010) 7611–7617.
- [81] L. Deng, M. Han, Microwave absorbing performances of multiwalled carbon

- nanotube composites with negative permeability, *Appl. Phys. Lett.* 91 (2007) 023119.
- [82] Z. Li, Y. Deng, B. Shen, W. Hu, Size influence on microwave properties of Ni–Co–P hollow spheres, *J. Phys. D Appl. Phys.* 42 (14) (2009) 145002.
- [83] P. Markos, C. Soukoulis, Transmission properties and effective electromagnetic parameters of double negative metamaterials, *Opt. Express* 11 (7) (2003) 649–661.
- [84] Z. Liu, G. Bai, Y. Huang, F. Li, Y. Ma, T. Guo, et al., Microwave absorption of single-walled carbon nanotubes/soluble cross-linked polyurethane composites, *J. Phys. Chem. C* 111 (37) (2007) 13696–13700.
- [85] R.C. Che, L.M. Peng, X.F. Duan, Q. Chen, X.L. Liang, Microwave absorption enhancement and complex permittivity and permeability of Fe encapsulated within carbon nanotubes, *Adv. Mater.* 16 (5) (2004) 401–405.
- [86] E. Michielssen, J.M. Sajer, S. Ranjithan, R. Mittra, Design of lightweight, broadband microwave absorbers using genetic algorithms, *IEEE Trans. Microw. Theor. Tech.* 41 (6) (1993) 1024–1031.
- [87] A. Jaiswal, R. Das, T. Maity, P. Poddar, Dielectric and spin relaxation behaviour in DyFeO₃ nanocrystals, *J. Appl. Phys.* 110 (12) (2011) 124301.
- [88] D.C. Sinclair, T.B. Adams, F.D. Morrison, A.R. West, CaCu₃Ti₄O₁₂: one-step internal barrier layer capacitor, *Appl. Phys. Lett.* 80 (12) (2002) 2153–2155.
- [89] Q. Li, X. Yin, W. Duan, B. Hao, L. Kong, X. Liu, Dielectric and microwave absorption properties of polymer derived SiCN ceramics annealed in N₂ atmosphere, *J. Eur. Ceram. Soc.* 34 (3) (2014) 589–598.
- [90] X.L. Dong, X.F. Zhang, H. Huang, F. Zuo, Enhanced microwave absorption in Ni/polyaniline nanocomposites by dual dielectric relaxations, *Appl. Phys. Lett.* 92 (1) (2008) 92.